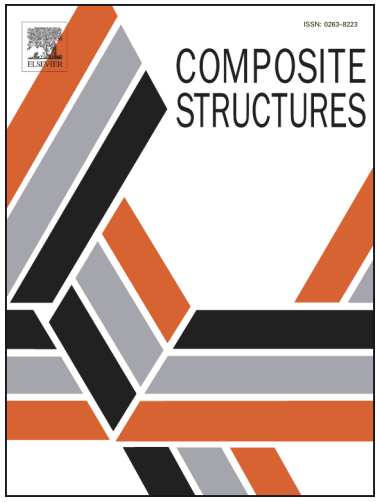

Experimental investigation on the mechanical behaviour of 3D carbon/carbon composites under biaxial compression

Chenghai Xu, Leying Song, Hanxing Zhu, Songhe Meng, Weihua Xie, Hua Jin

PII: S0263-8223(17)32333-4
DOI: https://doi.org/10.1016/j.compstruct.2017.11.035
Reference: COST 9101

To appear in: *Composite Structures*

Received Date: 27 July 2017
Accepted Date: 14 November 2017

Please cite this article as: Xu, C., Song, L., Zhu, H., Meng, S., Xie, W., Jin, H., Experimental investigation on the mechanical behaviour of 3D carbon/carbon composites under biaxial compression, *Composite Structures* (2017), doi: https://doi.org/10.1016/j.compstruct.2017.11.035

Experimental investigation on the mechanical behaviour of 3D carbon/carbon composites under biaxial compression

Chenghai Xu[a] Leying Song[a], Hanxing Zhu[b], Songhe Meng[a] *, Weihua Xie[a], Hua Jin[a]

[a]*Center for Composite Materials, Harbin Institute of Technology, Harbin, China*
[b]*School of Engineering, Cardiff University, Cardiff, UK*

ABSTRACT

The effects of complex state of stress on the compressive behaviour of 3D carbon/carbon composites are investigated by application of uniaxial and biaxial loadings using a specially developed Zwick cruciform testing facility. The shape of the biaxially loaded cruciform specimen is optimised to avoid premature fracture outside the gauge section. A semi-analytical method is proposed to determine the stress components in the gauge section of the biaxial specimen. The experimentally obtained failure stress relation, which traces an elliptical path in the principal stress space, can be well represented by the Tsai criterion with a stress interaction parameter of F_{12}=-0.85. Macro-fracture morphology and SEM micrographs are examined and the results show that the failure mechanisms of the composites vary with the loading ratio. The results also suggest that the biaxial stress interaction effect is represented by a domain in the biaxial specimen, which is characterised by torsion and bending fractures in the dislocated fibres between two adjacent Z yarns.

*Keywords:*A. Carbon-carbon composites(CCCs); B. fracture; C. mechanical properties;

*Corresponding author. Tel.:+86 451 86402343.
E-mail address: mengsh@hit.edu.cn (Songhe Meng).

D. fractography;

1. Introduction

Three-dimensionally reinforced carbon/carbon composites (3D C/C composites), one type of the most promising structural materials used in aviation, aerospace and the naval industry [1,2], have received increasing attention in recent years. Owing to the 3D reinforcement architecture, composites reinforced with such preforms exhibit excellent through-thickness properties, high fracture resistance, retention of strength and structural integrity at high temperatures [3,4]. Since the structural material in most applications is loaded under a multiaxial stress state, any small secondary loads could lead to failure when they coincide with a weakness in the material. Therefore, experimental investigation should consider multi- or bi-axial testing, which can be a foundation for the new design strategy to cope with the presence of multiple failure modes, depending on the loading direction and state of stress.

Currently, many studies have focused on the mechanical properties of 3D C/C composite under uniaxial loading, and the strength, failure mechanisms and damage tolerance have particularly been assessed [5,6]. Experimental investigations on the compression properties and failure mechanism of 3D braided composites by Li et al. [7] have shown that the damage and failure patterns of composites vary with the loading directions. For the longitudinal compression, failure occurs as the fibre bundles loosen. In the case of in-plane compression, the material is compacted gradually and damage builds up in the transverse direction. While, for the transverse compression, the material exhibits

shear fracture at a 45° angle. Kuo et al. [5] carried out compressive testing on 3D orthogonal composites, which were reinforced by interlacing loops containing one set of axial yarns and two sets of weaving yarns. They conclude that the bending fractures of axial yarns are found in the compressive tests and the yarn imperfection is the major failure-determining factor. Although the descriptions of the mechanical behaviours under compression can be found for some kinds of 3D C/C composites, more comprehensive understanding is highly desired to feature the compressive performance under different variations such as stress and defect sensitivity, reinforcement architecture, loading rate, confinement and mechanical properties of the matrix. Thus, compressive force has become one of the most critical loading conditions for 3D reinforcement composites [6].

In contrast, relatively few efforts have been made to study the mechanical performance under combined stress states for C/C composites [8,9], which can be due to the difficulty to physically load the specimen along the two axes. A lack of understanding of the mechanical behaviours under multi- or bi-axial loading has directly hindered the development of any reasonable predictive theory. In addition, it has been confirmed that there is a notable difference between the composites tested under combined stress states [10]. For instance, Budiansky and Fleck [11] have found a significant reduction in strength for unidirectional composites when applying a state of stress of combined shear and axial compression. Quek et al. [12] have identified the mode of failure for carbon 2D triaxial braided composites under biaxial tension/compression,

involving distributed matrix cracking and local tow buckling, which precipitates braid/matrix interfacial failure. In addition, failure mechanisms and stress-strain behaviours have been investigated for 2D laminates composites under in-plane biaxial compression [13,14]. Potter et al. [13] have reported that failure modes with an increasing loading confinement ratio for fibre orientation transition from the uniaxial failure mode of in-plane shearing to out-of-plane shearing and massive delamination for graphite-epoxy (AS4/3502) laminates. Grape et al. [14] have determined the mechanical behaviour of 2D C/C woven laminates under in-plane biaxial compression loads, by varying the biaxial stress ratio R. The results show that two shear faults aligned with the axes of loading are formed for R>75%, whereas for R<75%, only one fault is observed. However, few investigations on the biaxial compressive mechanical responses and the failure mechanisms influenced by biaxial compressive loading ratios are found for 3D carbon/carbon composites, which are expected to behave differently from their 2D counterparts.

This work presents a comprehensive experimental investigation on the mechanical behaviors of 3D C/C composites under uniaxial and biaxial compressive loadings. The aim is to explore the effects of complex state of stress on the strength and failure mechanisms of 3D C/C composites under different loading ratios. Section 2 provides details on the material systems used, the 3D C/C composites and their microstructural characteristics. Section 3 describes the details of experimental procedure for uniaxial and biaxial compression tests. Specifically, a semi-analytical method is proposed for the

determination of the biaxial compressive stress components and failure stresses in the gauge section based on the shape factor. In addition, an optimised specimen shape is adopted to ensure that failure always occurs in the gauge section. Section 4 presents the results of the mechanical responses under the compression with five different loading ratios. The typical stress-strain curves and interaction failure stress envelope are obtained. The fracture morphology is observed from the macroscopic and microscopic views, and the main failure mechanism is demonstrated. In addition, the influences of stress states with different loading ratios on the compression properties and failure modes are analysed. Section 5 summarises the main work done in this paper.

2. Material systems

The 3D carbon/carbon (C/C) composites used in this study are processed by chemical vapour infiltration of a pyrocarbon matrix into a fibrous preform with ex-PAN carbon-fibre. The preform architecture consists of eight-harness satin woven layers in a symmetric (0º/90º) layup, which are stitched together with yarns in the thickness direction. The described fabric architecture makes the properties in the 0º direction the same as those in the 90º direction. The densification process of the 3D C/C preform by isothermal CVI is performed, followed by heat treatment at a temperature of 2100-2300℃ for graphitisation. The final fibre volume fraction of the C/C composites is 56% and the total porosity of the material is less than 5%.

A typical microstructure in the cross-section normal to the weft/warp tow direction

of the 3D C/C composites is obtained using an optical microscope and shown in Figure 1. It features eight-harness satin woven fabric in plane with the same tow count in the weft and warp directions and periodically stitched yarns perpendicular to the plies. The crimps at the intersection of the weft tow and warp tow on the same level are formed and the mean crimp angle is about 8°, which is obtained from at least 30 measurements along the weft direction. The defects are identified as voids and cracks, in both the intra-tow and inter-tow, as shown in Figure 1(b). The large voids are usually embedded in the matrix-rich pockets due to the formation of gaseous hydrocarbons during the carbonisation process. The cracks are formed due to the residual stress generated from the changes in temperature during the process. The defects can be a cause of substantial perturbations in the mechanical responses.

3. Experimental procedure

3.1. Uniaxial compression

3.1.1. Test procedure

Figure 2(a) shows the shape and dimensions of specimen designed for uniaxial tests. The dog-bone-shape can successfully prevent premature bending deformation at the ends. The specimen dimensions are designed to avoid any macroscopic buckling and to provide a good distribution of the flaws inherent in the microstructure. All the specimens for uniaxial loadings are cut from the same part of the 3D C/C composite to minimise the material discrete influence due to different batches. In addition, special care has been

taken when cutting the sample to ensure the tows either along the x-axis or y-axis loading direction. The loading surfaces of the specimens are subsequently ground and polished to a mirror finish.

At least five similar specimens are prepared and tested for each test condition in order to quantify the accuracy of the measurement. The specimens are loaded at a cross-head speed of 0.5 mm/min using the biaxial testing machine and more details are provided later. Longitudinal and transversal deformations are measured using resistance strain gauges mounted on the front and rear faces. The load-strain data are registered until failure occurs.

3.1.2. Data processing

A chord modulus is determined over a range of axial strain from 800 to 1200 microstrain, representing the linear lower half of the stress-strain curve. The compressive modulus is obtained using Equation

$$E = \frac{\Delta P^u}{b \cdot d \cdot \Delta \varepsilon^u} \quad (1)$$

Where E is in MPa; ΔP^u is the change in the applied force between two loading points of the linear part of the load-strain curve, N; $\Delta \varepsilon^u$ is the corresponding change in the compressive strain between the same two loading points; b is the width of the specimen; and d is thickness of the specimen; and superscript u indicates the uniaxial compressive loading condition.

The Poisson ratio is determined using the same loading range to obtain the

transverse strain, and given as

$$\nu_{ij} = \frac{\Delta\varepsilon_i^{\,u}}{\Delta\varepsilon_j^{\,u}} \tag{2}$$

Where $\Delta\varepsilon_i^{\,u}$ is the change in transverse strain between the two loading points; and $\Delta\varepsilon_j^{\,u}$ is the change in longitudinal compressive strain between the same two loading points.

The compressive failure stress of the composite under uniaxial loading is obtained as

$$F^u = \frac{P^{u,\max}}{b \cdot d} \tag{3}$$

Where F^u is in MPa; and $P^{u,\max}$ is the maximum force before failure, N.

3.2. Biaxial compression

3.2.1. Biaxial compression apparatus

All biaxial tests are conducted using a Zwick cruciform testing facility developed for this study, as shown in Figure 3. Its major components are two orthogonal pairs of axially aligned load cells, i.e. force-measuring device, run by four sets of 50kN electromechanical spindle drives. The system allows both displacement and force control of the individual axes, attaining a wide extent of biaxial loading ratios. This loading scheme is able to unload immediately when any instable fracture is detected to ensure minimum post-failure damage of the specimen. A custom-made jig is used during the biaxial compressive test, as shown in Figure 3(b), and a schematic diagram is shown in Figure 3(a). Ground, polished and hardened steel inserts are used between the adapters

and the specimen to ensure that the loaded surfaces of the specimen are smooth without micro-indentations caused by inserts. In order to avoid interference between two adjacent components, the width of the platen is chosen as 20 mm, which is 80% of the specimen width.

3.2.2. Test specimen

According to previous work by Smits [15], in addition to satisfying the required conditions for uniaxial compression, the geometry of the biaxial specimens has to satisfy the following conditions: (i) Maximisation of the region of uniform biaxial strain; (ii) Minimisation of the shear strains in the biaxial load testing zone; (iii) Minimisation of the strain concentrations outside the testing zone; (iv) Specimen failure in the biaxial load testing zone; (v) Repeatable results. Thus, the geometry of the biaxial specimen is optimised accordingly and presented schematically in Figure 2(b), which has in-plane dimensions of 25mm×25mm, with a chamfer at each of the four corners to relieve stress concentrations and is milled in the central regions of the symmetry planes through the thickness to make a greater stress level in the (gauge) testing zone. Note that the specimens are cut parallel to the weft and warp tows so that the test results are related directly to the mechanical properties along the material principal directions. The sample surfaces are subsequently ground and polished to reduce the surface residual stress. It is important that the ends of the specimen are machined flat, parallel to each other and perpendicular to the long axis of the coupon.

3.2.3. Test procedure

A constant force loading rate of 10N/s is applied along the principal axis (x-axis) and the loading rate of the secondary axis (y-axis) is fixed through the feedback control systems, keeping a prescribed biaxial loading ratio, i.e., the ratio of the load applied on the secondary axis to that on the primary axis, $R = \sigma_y / \sigma_x$. All tests are performed at the room temperature and back-to-back strain measurement is made for a correction of testing errors because of any bending of the specimen. At least five specimens are prepared and tested for each testing case. Moreover, in all biaxial tests, the two stresses increased simultaneously as did the corresponding strains, keeping the ratio unchanged. With a view to understanding the effects of different biaxial loading ratios, five loading cases were performed on the 3D C/C composite, including one uniaxial compression test and four biaxial compression tests, that is R=0, 0.2, 0.33, 0.5 and 1, respectively.

3.2.4. Data processing

Strain gauges are placed in a rosette pattern in the central surface, which is designed following the principles described above along the directions of the compressive loads. The load, strain and mode of damage at specific points are registered. A semi-analytical method based on the phenomenological shape factor is proposed to determine the stress components in the specimen gauge, and given as

$$\sigma_x^b = \frac{E_x \varepsilon_x^b + E_x \nu_{xy} \varepsilon_y^b}{1 - \nu_{xy} \nu_{yx}}, \quad \sigma_y^b = \frac{E_y \varepsilon_y^b + E_y \nu_{yx} \varepsilon_x^b}{1 - \nu_{xy} \nu_{yx}} \tag{4}$$

Where E_x, E_y, ν_{xy} and ν_{yx} are the material elastic constants in the corresponding

axes, which are treated as material eigenvalues obtained from the uniaxial compression test. σ_x^b, σ_y^b, ε_x^b and ε_y^b are the stress and strain components in the corresponding axes, respectively. The superscript *b* indicates a biaxial compressive loading condition, while the subscripts *x* and *y* stand for the directions of the stresses or strains.

The stress components in the gauge section can be obtained from the force in the same axis and the shape factor which defines the effective gauge cross-sectional area of a flat cruciform specimen in the specific direction. According to the concept of stress, it can be concluded that the shape factors are variables only depending on the specimen's geometry and are irrelevant to the loading case. Thus, the shape factors have the same dimension as area. The relations can be expressed as

$$P_x^b = N_x^b \sigma_x^b, \quad P_y^b = N_y^b \sigma_y^b \tag{5}$$

Where P_x^b and P_y^b are the two primary axis forces measured by the load cells of the biaxial test facility. N_x^b and N_y^b are the shape factors of the *x* and *y* axes, respectively.

Combining Equations (4) and (5), the analytical relations between the loads and strains in the principal axes can be obtained as

$$P_x^b = N_x^b \frac{E_x \varepsilon_x^b + E_x \nu_{xy} \varepsilon_y^b}{1 - \nu_{xy} \nu_{yx}}, \quad P_y^b = N_y^b \frac{E_y \varepsilon_y^b + E_y \nu_{yx} \varepsilon_x^b}{1 - \nu_{xy} \nu_{yx}} \tag{6}$$

The shape factors can be determined using the method of linear regression based on the measuring data of forces and strains from the biaxial compressive tests. In this paper, the shape factors of the adopted biaxial specimen are obtained as $N_x^b = N_y^b = 74.14 mm^2$. Therefore, the stress components and the failure stresses can be calculated accordingly.

4. Results and discussion

4.1. Stress-strain response

Data are collected from valid experimental tests, with the final failure of the specimen occurring within the gauge section. A typical stress-strain curve of the composites under uniaxial compression is shown in Figure 4(a). The stress-strain response shows a toe region, as indicated in Block I in the uniaxial compressive loading history, caused by a take-up of slack and alignment or seating of the specimen according to the analysis of ASTM D 695-2010. The stress-strain response becomes linear in Block II, and the elastic constants of the composites are calculated based on the slope of the load history in this block. Using Equations (1) and (2), the Young's moduli in the *x*-direction and the *y*-direction can be obtained as $E_x=E_y=58.43$ GPa and Poisson ratio as $\gamma_{xy}=0.2233$. The compressive behaviour in Block III of the stress-strain curve is slightly non-linear, which is attributed to damage accumulation. The final failure of the 3D C/C composites under the uniaxial compression is brittle and catastrophic.

Two typical stress-strain curves under biaxial compression with different loading ratios R=0.5 and R=1 are shown in Figures 4(b) and 4(c), respectively. Following the constant load ratios of the compressive loading in the *x*- and *y*- directions, the two curves have similar trends, including similar Poisson effects at the initial stage, as shown in Figure 4(c) with R=1. It is observed that a more significant Poisson effect exhibits in the curve, which reflects the behaviour in the *y*-axis, a lower stress level direction, shown in Figure 4(b) with R=0.5. That is, the Poisson effect is somewhat reduced in magnitude

along the *x*-axis, but is significantly increased along the *y*-axis with increasing R. In the next stage, a material exhibits a region of linear behaviour in both directions, after which damage nucleates and propagates in complex modes and a typical brittle failure can be observed.

4.2. Failure stress

Figure 5 plots the typical failure stresses vs. the loading ratio of 3D C/C composites under biaxial compressive tests, where the error bars indicate a scatter of the standard deviation of the data. In addition, Table 1 shows the values of the 3D C/C failure stresses under compression in both the *x* and *y* directions. As can be seen from Figure 5(a), the failure stresses in the orthogonal principal axes of 3D C/C are functions of the loading ratio, and the failure stresses in both directions monotonically increase with the loading ratio. For the case in the y-axis, the compressive failure stress increases linearly with the loading ratio and reaches the full carrying capacity when R=1. In contrast, the compressive failure stress in the x-axis when R=1 is over 1.25 times the uniaxial compressive failure stress. It is suggested that the gradually enhanced failure stress in the x-axis is caused by the reduced out-of-plane shearing failure mode with increasing R. Since increasing the loading in the y-axis raises the normal and in-plane stresses of the 3D C/C and reduces the out-of-plane shear stresses in the interface between matrix and fibres in longitudinal and transverse directions, critical stresses to initiate failure via the latter failure mechanisms occur before the shear strength is reached. The transitions of primary

failure modes will be detailed in Section 4.3.

The combined compressive stress state caused an increase in the strength, with a resulting elliptical failure surface in the compression-compression stress space, as shown in Figure 5(b). The Tsai criterion [16], which is the theory proved to be applicable to most of the tests in the 'exercise' [17], is used to represent the biaxial compressive fracture envelope in the σ_{11}-σ_{22} stress space, where biaxial stress interaction is emphasised. The criterion is defined as

$$\left(\frac{\sigma_1}{X_T X_C}\right)^2+\left(\frac{\sigma_2}{Y_T Y_C}\right)^2+\left(\frac{1}{X_T}-\frac{1}{X_C}\right)\sigma_1+\left(\frac{1}{Y_T}-\frac{1}{Y_C}\right)\sigma_2+\left(\frac{2F_{12}\sigma_1\sigma_2}{\sqrt{X_T X_C Y_T Y_C}}\right)+\left(\frac{\tau_{12}}{S_{12}}\right)^2=1 \quad (7)$$

Equation (7) contains five basic strength material constants, namely, the longitudinal tensile strength X_T, the longitudinal compression strength X_C, the transverse tensile strength Y_T, the transverse compression strength Y_C, and the in-plane shear strength S_{12}. In addition, the equation includes one parameter defining the biaxial stress interaction, F_{12}. The basic strength values are provided in Table 1 with the same values in tension and compression in the x and y directions. The remaining free parameter F_{12} can be calibrated according to the experimental database. The choice of F_{12}=-0.85 results in good agreement with the experimental observation, as shown in Figure 5(b). This specific value and the comparison with the maximum-stress failure criterion (Fig. 5(b)) clearly exhibit strong interaction between the two loading directions.

4.3. Failure mechanism

The morphology of fractures is examined using photographs and a scanning electron

microscopy from the macroscopic and microscopic view in order to investigate the type of damage and the failure mechanisms of composites. Figure 6 shows the typical fracture photographs of uniaxial and biaxial compression samples with R=0, 0.5, 1. As details show in Figures 6(a) and (b), a through-thickness shear-fault aligned with the loading direction is formed and eventually leads to complete unloading of the load train. Interply delamination and fibre fracture occur due to fibres buckling, especially arising from the localisation of bending strains at the crimps in the fibre architecture. Compared to uniaxial compression (R=0), increasing the loading ratio to 0.5 reduces the number of transverse cracks and the extent of delamination, as indicated in Figure 6(c). A loading ratio of 1 causes extensive complex but intriguing damage modes (Figure 6(d)), which can be divided into three domains according to the primary fracture modes, namely, D-I, D-II and D-III for clear description. In D-I and D-III, the fracture modes are closely related to the compressive loading directions. While in D-II, those are associated with both the compressive stress interactions from the two orthogonal directions and the intersections of yarns. The transition of fracture modes is due to the variation of stress component distribution with increasing loading ratio. This stress tilts the maximum matrix shear plane in the out-of-plane direction as the y-axis stress increases and, in addition, more interaction effect between the two directional stresses can be observed when the two primary directions have roughly equal stress, i.e. R=1.

Figure 7 shows the SEM photograph of composites compressed under uniaxial loading in the x direction, i.e. R=0. From a side view in Figure 7(a) and (b), for the pure

uniaxial compression, the fractured pieces act like wedges with a fracture angle of about 45°, between the fractured surface and the thickness direction. On the edge of the thickness direction, severe delamination caused by transverse tow cracking and longitudinal fibre bundle fracture can be observed. Figure 7(c) shows the elevation view of the fracture surface to further examine the fracture mechanisms of each directional yarn. The damage is propagated by cracking of the interface between fibres and the matrix and the fibres shear fracture is shown in the load-aligned tows in Figure 7(e), 7(f) and 7(g). Contrary to the damage type for a 2D composite under the same loading condition [18], few kink bands can be found due to the pinning effect for the presence of yarns in the thickness direction. The transverse tows show slight bending fractures, associated with delamination between the tows and matrix near the crimp regions. Within the transverse tows, transverse cracking between fibres and several fibre breaks can also be observed, as shown in Figure 7(h), 7(i) and 7(j). Z-tows behave as structural elements at the reinforcement level damaged with pull-put tows, as indicated in Figure 7(d). Also, splitting between fibres in the remaining Z-tows can be observed.

Figure 8 is a typical micrograph of 3D C/Cs, showing the fracture surface with R=0.5. No obvious wedge-like fracture can be found in the fractured samples, i.e. there is a much smaller fracture angle presented in the case of R=0.5. Contrary to the form of shear fault due to the cracking path along the x tows in the case of R=0, the intra fibres cracking is preferred to the transverse directions with debonding within the x tows under R=0.5, as revealed in Figures 8(b) and 8(c). By observation of the fracture in the y tows

(in Figures 8(d), 8(e) and 8(f)), it can be seen that serious interfacial debonding occurs between the fibres and the matrix and the fibres generate pronounced bending fractures near the crimp regions.

According to the observation of macroscopic graphs with R=1, the fracture surface can be roughly divided into three domains as defined above. In D-I, shown in Figure 9(a), the composite shows shear fracture at about a 45°angle, the normal surface of which is perpendicular to the y-axis. From detailed observation of Figure 9(b), the fibres in the shear plane in the x tows are torn, and cracks transfer intra the x-tows with debonding between the fibre and the matrix. Moreover, fibre breakage in bending is noticeable in the y tows, which is revealed in Figure 9(c) and detailed in Figure 9(d). In addition, the z fibre bundles are pulled out as a whole. Considering the typical fracture mechanisms with R=0, the composite breaking in D-I with R=1 is similar to that under uniaxial compression in the x direction. In D-II, SEM observations show that many twists and breakages can be found within dislocated fibres (Figures 9(e) and 9(f)), which clearly imply the strongly interactive effect by the two orthogonal loading directions under biaxial compression with R=1, which is also the reason for the strength envelope in the normal stress space presented in Section 4.2. Compared with the fracture modes in D-I, those in D-III can be explained in the same way, except in the mutual vertical loading direction. In addition, severe splitting between fibres within the z tow can be observed in Figures 9(g) and 9(h).

5. Conclusion

The compressive properties of 3D C/C composites under uniaxial and biaxial loading are experimentally studied. Five stress states are achieved through confined loading ratios on the developed Zwick cruciform testing facility. The optimised specimen shape with a chamfer at the corners and thickness reduction in the gauge regions developed for the biaxial testing facility can successfully avoid stress concentrations leading to premature fracture outside the gauge section. A semi-analytical method combined with experimental data based on the shape factor is proposed for the determination of the stress components in the gauge section, and hence the stress-strain curves and failure stresses are obtained. The failure stresses are improved with the increase of the loading ratios. The collection of uniaxial and biaxial failure stresses represents the elliptical fracture envelope, which can be well described by the Tsai criterion when the parameter of biaxial stresses interaction is F_{12}=-0.85.

The macro- and micro-fracture morphology examinations indicate that the failure mechanisms of the composites vary with the loading ratios. For the uniaxial case (R=0), the failure occurs as the shear fault cracks longitudinally along the interface between the load-aligned fibres and matrix and transverse fibre bending fractures. For R=0.5, a case representing the gradual increase of compression in the y-axis, a much smaller fracture angle can be observed caused by the cracking transverse in the interface between the longitudinal fibres and the matrix. As for R=1, the two directional compressive loadings are roughly similar, which results in a domain showing a clear interaction effect with twists and bending fractures in the dislocated fibres between two adjacent z yarns.

Acknowledgements

This work has been supported by the Natural Science Foundation of China (11472092) and the National Basic Research Program of China (973 program, No. 2015CB655200).

References

[1] Mouritz AP, Bannister MK, Falzon PJ, Leong KH. Review of applications for advanced three-dimensional fibre textile composites. Compos Part A Appl Sci Manuf 1999;30:1445–61.

[2] Huang ZM. The mechanical properties of composites reinforced with woven and braided fabrics. Compos Sci Technol 2000;60:479–98.

[3] Luo R, Liu T, Li J, Zhang H, Chen Z, Tian G. Thermophysical properties of carbon/carbon composites and physical mechanism of thermal expansion and thermal conductivity. Carbon N Y 2004;42:2887–95.

[4] Vettegren VI, Bashkarev AY, Barausov A V., Gabaraeva AD, Pikulin VA, Savitskiĭ A V. Temperature dependences of the strengths of a carbon fiber and a three-dimensional reinforced carbon-carbon composite. Tech Phys 2008;53:59–63.

[5] Kuo WS, Ko TH, Lo TS. Failure behavior of three-axis woven carbon/carbon composites under compressive and transverse shear loads. Compos Sci Technol 2002;62:989–99.

[6] Hatta H, Taniguchi K, Kogo Y. Compressive strength of three-dimensionally

reinforced carbon/carbon composite. Carbon 2005;43:351–8.

[7] Li D Sen, Zhao CQ, Ge TQ, Jiang L, Huang CJ, Jiang N. Experimental investigation on the compression properties and failure mechanism of 3D braided composites at room and liquid nitrogen temperature. Compos Part B Eng 2014;56:647–59.

[8] Greve L, Bisagni C, Walters CL. Biaxial experimental determination of in-plane matrix fracture envelope of unidirectional composite. Compos Part A Appl Sci Manuf 2010;41:750–8.

[9] Daggumati S, Van Paepegem W, Degrieck J, Praet T, Verhegghe B, Xu J, et al. Local strain in a 5-harness satin weave composite under static tension: Part II - Meso-FE analysis. Compos Sci Technol 2011;71:1217–24.

[10] Jelf PM, Fleck NA. The failure of composite tubes due to combined compression and torsion. J Mater Sci 1994;29:3080–4.

[11] Budiansky B, Fleck NA. Compressive failure of fibre composites. J Mech Phys Solids 1993;41:183–211.

[12] Quek SC, Waas A, Shahwan KW, Agaram V. Compressive response and failure of braided textile composites: Part 1 - experiments. Int J Non Linear Mech 2004;39:635–48.

[13] Potter D, Gupta V, Chen X, Tian J. Mechanisms-based failure laws for AS4/3502 graphite/epoxy laminates under in-plane biaxial compression. Compos Sci Technol 2005;65:2105–17.

[14] Grape JA, Gupta V. Failure mechanisms in laminated carbon/carbon composites under biaxial compression. Acta Metall Mater 1995;43:2657–65.

[15] Smits A, Van Hemelrijck D, Philippidis TP, Cardon A. Design of a cruciform specimen for biaxial testing of fibre reinforced composite laminates. Compos Sci Technol 2006;66:964–75.

[16] Liu KS, Tsai SW. A progressive quadratic failure criterion for a laminate. Compos Sci Technol 1998;58:1023–32.

[17] Soden PD, Hinton MJ, Kaddour AS. a Comparison of the Predictive Capabilities of Current Failure Theories for Composite Laminates. vol. 58. 1998.

[18] De Carvalho N V., Pinho ST, Robinson P. An experimental study of failure initiation and propagation in 2D woven composites under compression. Compos Sci Technol 2011;71:1316–25.

Figure captions

Fig. 1. Typical optical micrographs on the y-z section of 3D C/C composites: (a) at low magnification; (b) at high magnification.

Fig.2. Shape and dimensions of the test specimens: (a) uniaxial compression specimen; (b) biaxial compression specimen.

Fig.3. The developed Zwick cruciform testing facility for biaxial compression: (a) schematic of the loading system; (b) testing process.

Fig. 4. Representative stress vs. strain curves obtained in the x-axis and y-axis for composites: (a) under uniaxial compressive loading case, i.e. R=0; (b) under the case with R=0.5; (c) under the case with R=1.

Fig. 5. (a) Variations of failure stresses with the standard deviation in the x-axis and y-axis as a function of the biaxial loading ratio, R. (b) Biaxial compression interaction

failure stress data points obtained by uniaxial and biaxial testing, corresponding to the Tsai and maximum-stress fracture envelope.

Fig. 6. The fracture photographs of 3D C/C composite: (a) an elevation view under uniaxial compression; (b) a side view under uniaxial compression; (c) an elevation view under biaxial compression with R=0.5; (d) an elevation view under biaxial compression with R=1.

Fig. 7. SEM micrographs of 3D C/C specimen fractured in uniaxial compression: (a) fracture surface from the side view; (b) detailed description of transversal cracking and delamination; (c) fracture surface from the elevation view; (d) splitting in the z yarn; (e) longitudinal cracking in the x yarn; (f) magnification of one segment of shear fault; (g) fibre breakage in shear; (h) transversal cracking and bending fracture in the y yarn; (i) magnification of one segment of bending fracture; (j) fibre breakage in bending.

Fig. 8. SEM micrographs of 3D C/C specimen fractured in biaxial compression with R=0.5: (a) fracture surface from the elevation view; (b) transversal cracking in the x yarn; (c) magnification of one segment of (b); (d) interface debonding and fibre bending fracture in the y yarn; (e) magnification of one segment of (d); (f) fibre breakage in bending.

Fig. 9. SEM micrographs of 3D C/C specimen fractured in biaxial compression with R=1: (a) fracture surface from the elevation view of D-I; (b) cracking in the y yarn of D-I; (c) cracking in the x yarn of D-I; (d) magnification of fibre fracture in the x yarn; (e) fracture surface in the elevation view of D-II; (f) dislocated short fibres characterised by bending fracture between adjacent z yarns in D-II; (g) fracture surface from the elevation view of D-III; (h) splitting in the z yarn.

Table 1

The experimentally obtained failure stress of the 3D C/C composites under uniaxial and biaxial compressions.

Stress ratio R	Failure stress σ_{11} [MPa]	Failure stress σ_{22} [MPa]
0	141.17±8.75	/
0.20	158.04±9.42	32.15±6.31
0.33	174.73±16.30	58.62±10.48
0.50	171.16±14.03	93.25±9.83
1	177.61±3.12	172.01±10.71

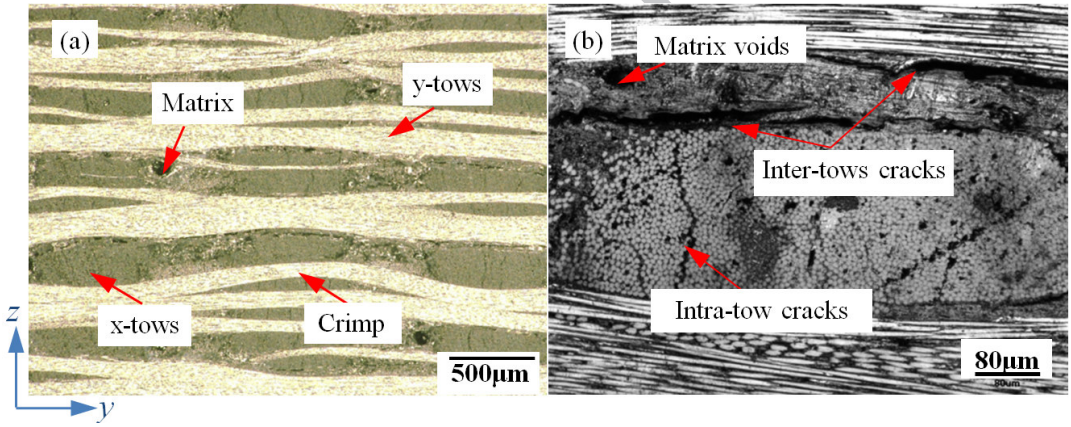

Fig. 1. Typical optical micrograph in the y-z cross-section of 3D C/C composites: (a) at low magnification; (b) at high magnification.

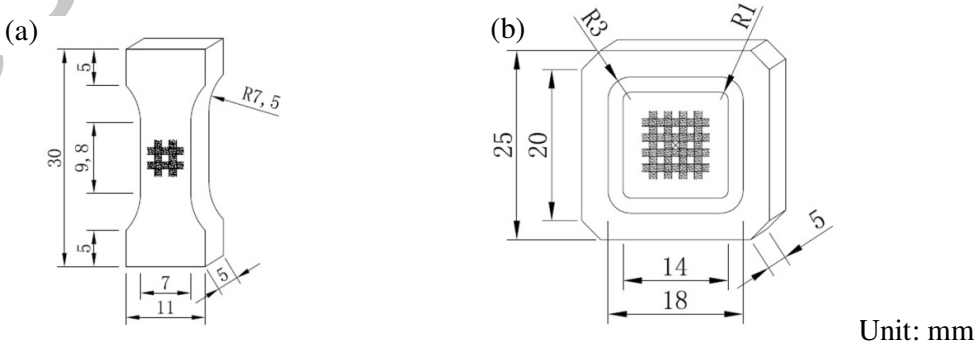

Fig.2. Shape and dimensions of the test specimens: (a) uniaxial compression specimen;

(b) biaxial compression specimen.

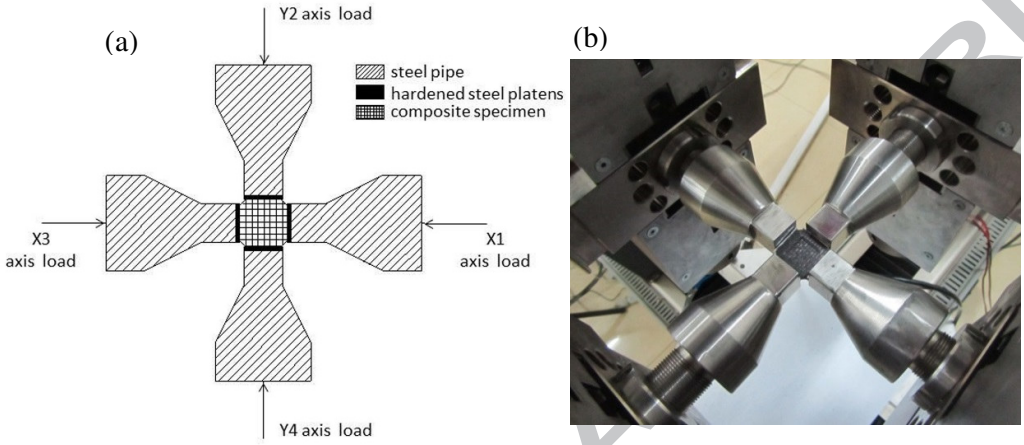

Fig.3. The developed Zwick cruciform testing facility for biaxial compression: (a) schematic of the loading system; (b) test process.

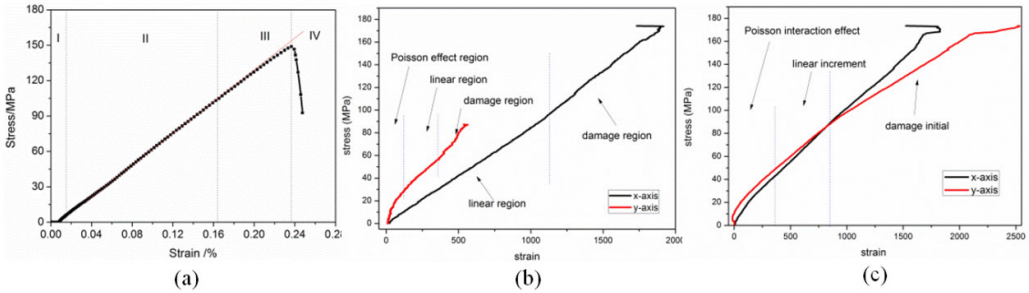

Fig. 4. Representative stress vs. strain curves obtained in the x-axis and y-axis for composites: (a) under uniaxial compressive loading case, i.e. R=0; (b) under the case with R=0.5; (c) under the case with R=1.

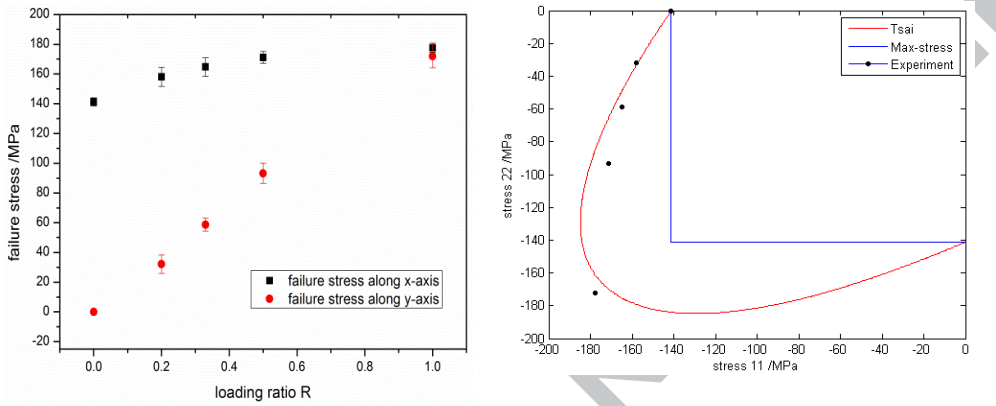

(a) (b)

Fig. 5. (a) Variations of failure stresses with the standard deviation in the x-axis and y-axis as a function of the biaxial loading ratio, R. (b) Biaxial compression interaction failure stress data points obtained by uniaxial and biaxial testing, corresponding to the Tsai and maximum-stress fracture envelope.

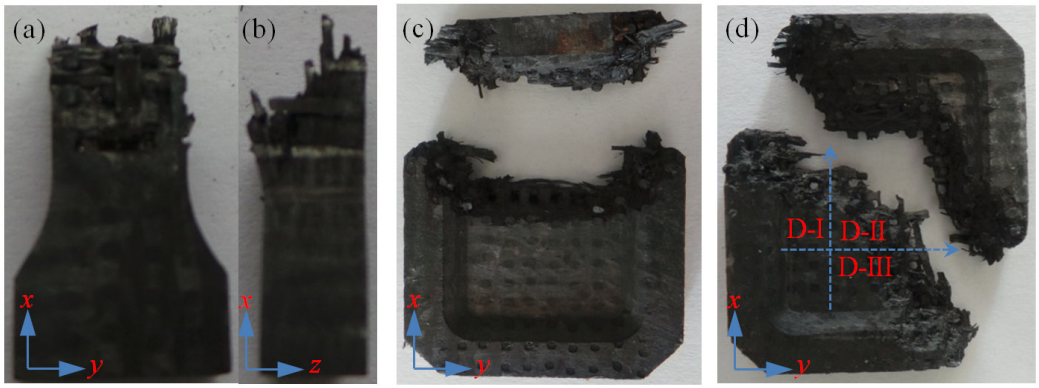

Fig. 6. The fracture photographs of 3D C/C composite: (a) an elevation view under

uniaxial compression; (b) a side view under uniaxial compression; (c) an elevation view under biaxial compression with R=0.5; (d) an elevation view under biaxial compression with R=1.

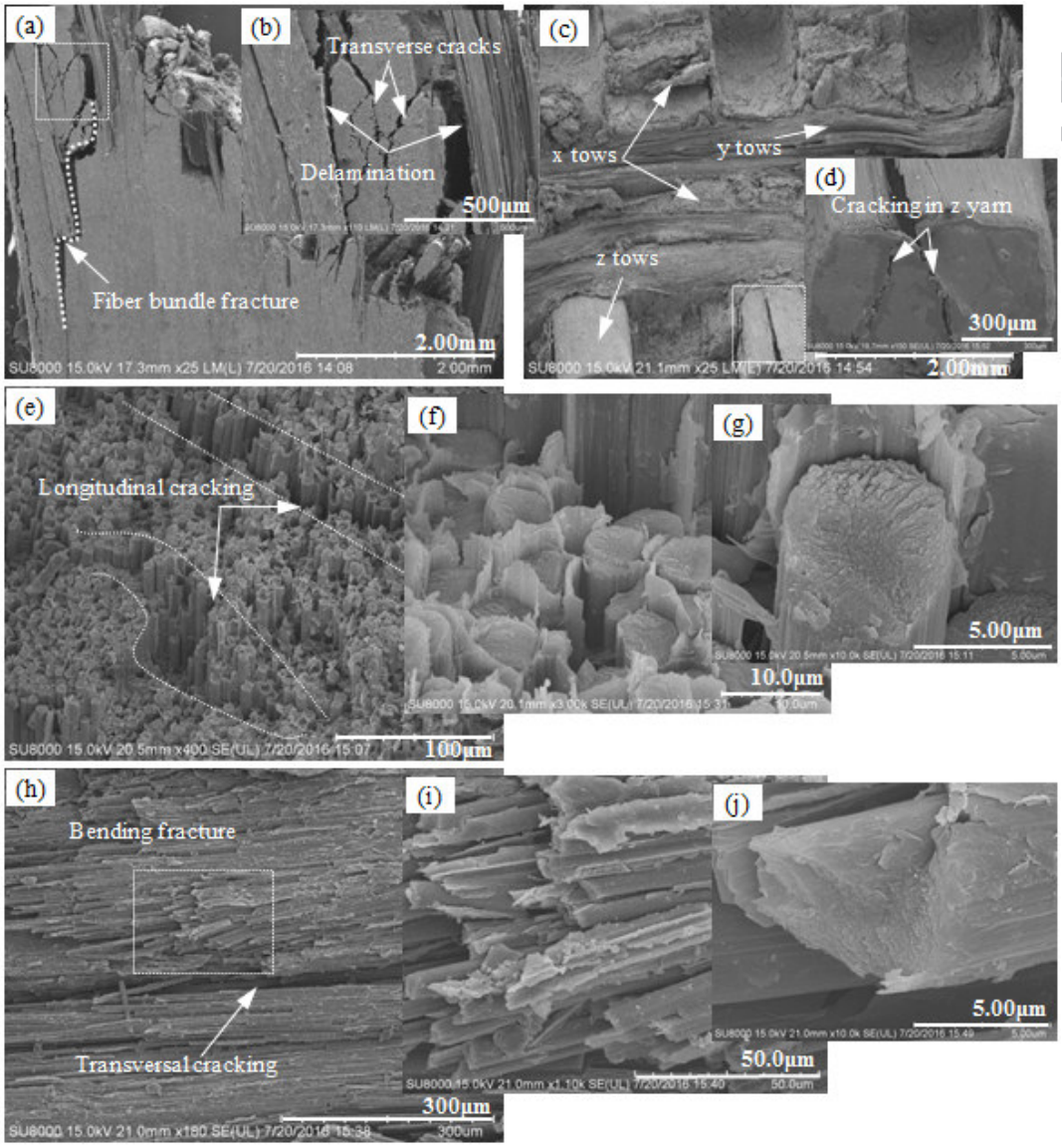

Fig. 7. SEM micrographs of 3D C/C specimen fractured in uniaxial compression: (a) fracture surface from the side view; (b) detailed description of transversal cracking and delamination; (c) fracture surface from the elevation view; (d) splitting in the z yarn; (e) longitudinal cracking in the x yarn; (f) magnification of one segment of shear fault; (g) fibre breakage in shear; (h) transversal cracking and bending fracture in the y yarn; (i)

magnification of one segment of bending fracture; (j) fibre breakage in bending.

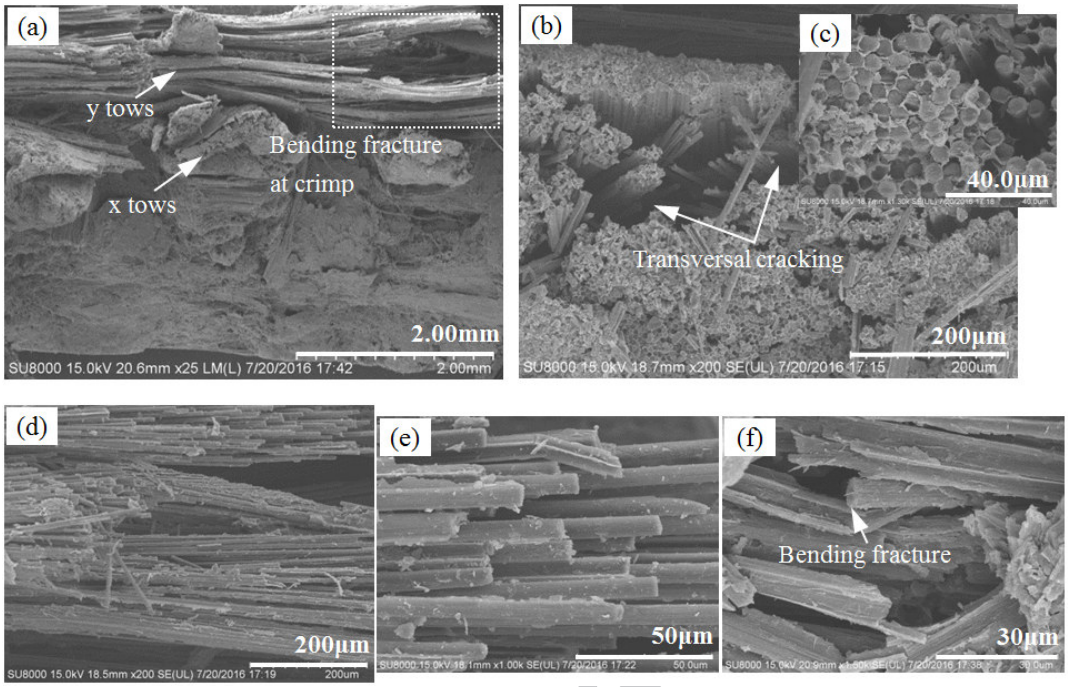

Fig. 8. SEM micrographs of 3D C/C specimen fractured in biaxial compression with R=0.5: (a) fracture surface from the elevation view; (b) transversal cracking in the x yarn; (c) magnification of one segment of (b); (d) interface debonding and fibre bending fracture in the y yarn; (e) magnification of one segment of (d); (f) fibre breakage in bending.

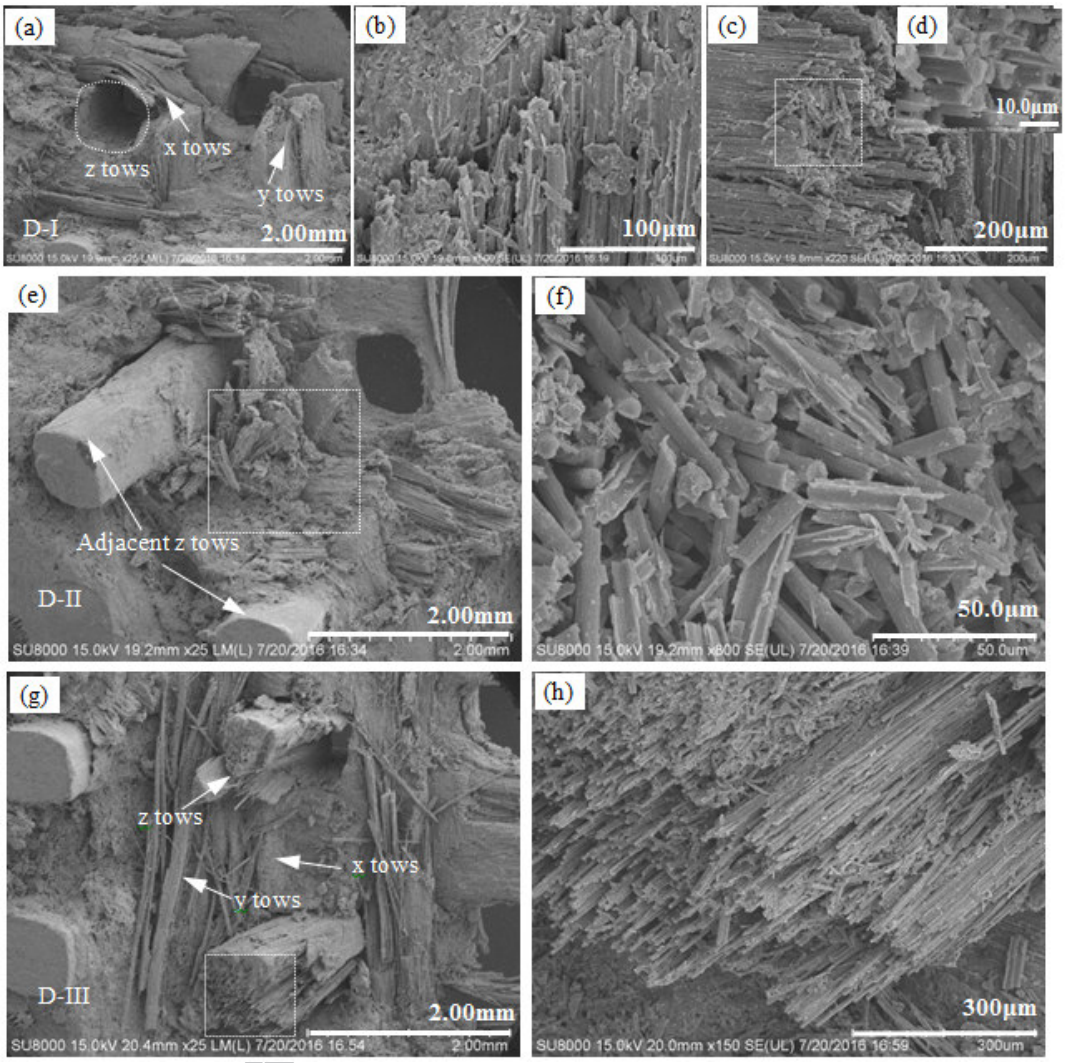

Fig. 9. SEM micrographs of 3D C/C specimen fractured in biaxial compression with R=1: (a) fracture surface from the elevation view of D-I; (b) cracking in the y yarn of D-I; (c) cracking in the x yarn of D-I; (d) magnification of fibre fracture in the x yarn; (e) fracture surface in the elevation view of D-II; (f) dislocated short fibres characterised by bending fracture between adjacent z yarns in D-II; (g) fracture surface from the elevation view of D-III; (h) splitting in the z yarn.